Engineering firecracker-like beta-manganese dioxides@spinel nickel cobaltates nanostructures for high-performance supercapacitors

Min Kuang [a], Zhong Quan Wen [b], Xiao Long Guo [a], Sheng Mao Zhang [c], Yu Xin Zhang [a, b, *]

[a] College of Materials Science and Engineering, Chongqing University, Chongqing 400044, PR China
[b] National Key Laboratory of Fundamental Science of Micro/Nano-Devices and System Technology, Chongqing University, Chongqing 400044, PR China
[c] Laboratory for Special Functional Materials, Henan University, Kaifeng 475004, PR China

HIGHLIGHTS

- $NiCo_2O_4$ nanosheets were decorated on β-MnO_2 nanowires by a facile and large-scale method.
- The firecracker core—shell architecture exhibited a high capacitance of 343 F g^{-1}.
- Excellent cycling stability: 95% capacitance retention after 3000 cycles.
- The asymmetric supercapacitor yielded a maximum power density of 2.5 kW kg^{-1}.

GRAPHICAL ABSTRACT
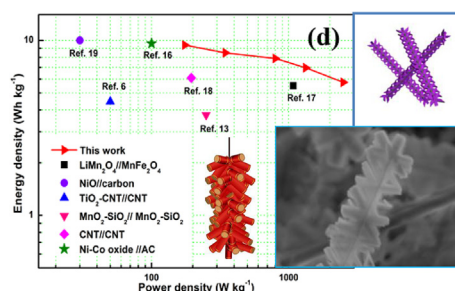
ABSTRACT

An effective and rational strategy is developed for large-scale growth of firecracker-like Ni-substituted Co_3O_4 ($NiCo_2O_4$) nanosheets on β-MnO_2 nanowires (NWs) with robust adhesion as high-performance electrode for electrochemical capacitors. The $NiCo_2O_4$—MnO_2 nanostructures display much higher specific capacitance (343 F g^{-1} at current density of 0.5 A g^{-1}), better rate capability (75.3% capacitance retention from 0.5 A g^{-1} to 8 A g^{-1}) and excellent cycle stability (5% capacitance loss after 3000 cycles) than Co_3O_4—MnO_2 nanostructures. Moreover, an asymmetric supercapacitor based on $NiCo_2O_4$—MnO_2 NWs as the positive electrode and activated graphenes (AG) as the negative electrode achieves an energy density of 9.4 Wh kg^{-1} and a maximum power density of 2.5 kW kg^{-1}. These attractive findings suggest this novel core—shell nanostructure promising for electrochemical applications as an efficient supercapacitive electrode.

© 2014 Elsevier B.V. All rights reserved.

1. Introduction

Supercapacitors are one class of energy storage systems that have attracted tremendous attention due to their superior advantages including high power/energy density, excellent cycling stability and fast charge/discharge capability [1]. Compared with secondary batteries, supercapacitors can provide high power in short-term pulses and be used as peak power sources in hybrid electric vehicles, memory backup devices, and back-up supplies to protect against power disruption [2]. On the basis of energy storage mechanism, there are two types of supercapacitors, namely electrical double-layer capacitors (EDLCs) and pseudocapacitors [3]. Recent research efforts have been made by exploiting novel electrode materials for supercapacitors with both high energy density and power density. Transition metal oxides, such as RuO_2 [4], MnO_2

[5,6,7,8], NiO [9], Co_3O_4 [5,10,11] and TiO_2 [8,12,13,14], contribute pseudocapacitance, although most of them suffer from low abundance, high cost for their raw materials, low electrical conductivity, and poor rate capability and reversibility during the charge–discharge process.

Recently, a ternary metallic oxide, spinel nickel cobaltite ($NiCo_2O_4$), has drawn much research interest [15,16,17,18,19]. The higher electrochemical capacitive performances may mainly derive from the superior electrochemical activity of $NiCo_2O_4$. More significantly, it is reported that $NiCo_2O_4$ possesses a much better electronic conductivity, at least two orders of magnitude higher, and higher electrochemical activity than nickel oxides and cobalt oxides [20,21,22,23]. For example, Wang and co-workers [23] obtained nickel cobaltite nanowires on carbon cloth with a specific capacitance of 245 F g^{-1} at 1 A g^{-1}. Liu et al. [16] reported that $NiCo_2O_4$@$NiCo_2O_4$ core/shell nanoflake array showed a specific capacitance of 1.55 F cm^{-2} at 2 mA cm^{-2}. Jiang et al. [21] synthesized the hierarchical porous $NiCo_2O_4$ nanowires which exhibited a specific capacitance of 743 F g^{-1} at 1 A g^{-1}. Very recently, rational design of multicomponent combination or mild methods has been applied to improve the specific capacitance of supercapacitors, which can provide the synergistic effect of all individual constituents, as well as efficient and rapid pathways for ion and electron transport (at their surfaces and throughout the bulk of the chemical distributions) [8,9,16]. In addition, manganese oxides (MnO_2), characterized by a low-cost material with a large theoretical capacity, abundant and environmentally friendly nature, have attracted significant interest as a promising alternative electrode material for supercapacitors [6,7,8]. It has been reported that, one-dimensional nanomaterials can facilitate the electrical transport along the axial direction, while maintaining high external surface area and thus high capacitance at fast charging-discharging rates [4,6,9]. To the best of our knowledge, there is little work on rational design of firecrackers-like $NiCo_2O_4$–MnO_2 NWs composite material for supercapacitors.

In this work, we develop a cost-effective and simple strategy to design and fabricate novel firecrackers-like $NiCo_2O_4$–MnO_2 NWs as an electrode for high-performance supercapacitors. The morphology, structure and electrochemical properties of the firecrackers-like $NiCo_2O_4$–MnO_2 NWs were investigated. Remarkably, due to their 1D nanoporous nanosheet microstructure and higher electrical conductivity compared with Co_3O_4–MnO_2 NWs, these $NiCo_2O_4$–MnO_2 NWs manifest a high specific capacity of 343 F g^{-1}, excellent cycling stability and high rate capability. Furthermore, an asymmetric supercapacitor device based on $NiCo_2O_4$–MnO_2//AG is assembled, which shows a maximum energy density of 9.4 Wh kg^{-1} and a maximum power density of 2.5 kW kg^{-1}.

2. Experimental

2.1. Material synthesis

All reagents were of analytical purity and used without any further purification. MnOOH NWs were prepared by a hydrothermal method. In a typical procedure, a 37 mL suspension containing the 297 mg manganese dioxide, together with 2 mL ethanol was made. Then the solution was transferred into a 50 mL stainless-steel autoclave and heated at 120 °C for 24 h, and then naturally cooled down to room temperature. The products were collected by filtration, washed with deionized water and ethanol, and finally dried at 60 °C for 12 h. The obtained MnOOH NWs were re-dispersed into 80 mL of ethanol and sonicated for 20 min to reach good dispersion. Afterward, 1.0 mmol nickel nitrate ($Ni(NO_3)_2$), 2.0 mmol cobalt nitrate ($Co(NO_3)_2$), 2 mmol ammonium

fluoride (NH_4F) and 5 mmol urea were dissolved in 80 mL DI water to form a transparent pink solution. The above two solutions were then mixed and heated to 90 °C in an oil bath for 8 h. After the solution was cooled down to room temperature naturally, the product was collected through centrifugation and washed with DI water and ethanol for several times. The products were then dried, followed by annealing at 300 °C for 2 h with a slow heating rate of 1 °C min^{-1} in order to get well-defined crystallized $NiCo_2O_4$–MnO_2 NWs hybrid structure. For comparison, Co_3O_4–MnO_2 nano-structures were synthesized through a similar route and subsequent annealing in air atmosphere. For the direct growth of Co_3O_4 nanosheets on MnO_2 NWs, single $Co(NO_3)_2$ salt was added into the reaction solution instead of the $Ni(NO_3)_2$ and $Co(NO_3)_2$. Except for the above parameters, the rest were the same as that of the synthesis of $NiCo_2O_4$–MnO_2 NWs.

2.2. Materials characterization

The crystallographic information of as-prepared products was established by powder X-ray diffraction (XRD, D/max 1200, CuKα). The structure and morphology of the products were carried out with focused ion beam scanning electron microscopy (ZEISS AURIGA FIB/SEM) and transmission electron microscopy (TEM, ZEISS LIBRA 200). Nitrogen adsorption–desorption isotherms were obtained using a micromeritics ASAP 2020 sorptometer.

2.3. Electrochemical measurements

The working electrode was prepared by mixing 80% active materials, 10% carbon black, and 10% polyvinylidene fluoride (PVDF) in N-methyl-2-pyrrolidone (NMP) and the slurry was spread onto a foam nickel current collector (1×1 cm^2). The electrode was heated at 120 °C for 10 h to evaporate the solvent and then uniaxially pressed under 10 MPa. The electrochemical tests of various samples were first conducted using a three electrode system in 2 M KOH using the CHI 660E electrochemical workstation. The reference electrode was an Ag/AgCl electrode and counter electrode was a Pt plate. Typically, the loading mass of active material was around 2.8 mg. The positive electrodes were investigated by cyclic voltammetry (CV) technique with varying the scan rate of 5–100 mV s^{-1} at potential between 0 and 0.5 V. Galvanostatic charge–discharge (GCD) experiments were performed with current densities ranged from 0.5 to 8 A g^{-1} at a potential of 0–0.43 V. The electrochemical impedance spectroscopy (EIS) was conducted in the frequency range between 100 kHz and 0.01 Hz with a perturbation amplitude of 5 mV versus the open-circuit potential.

For the tests with a two-electrode configuration, two slices of electrode material with the same size were assembled together with filter paper soaked in 2 M KOH solution before being connected to the potentiostat. In the two-electrode system, $NiCo_2O_4$–MnO_2 NWs and activated graphenes (AG) were the positive electrode and negative electrode, respectively. CVs were recorded as scan rates of 5, 10, 20, 40, 60 and 100 mV s^{-1}. GCD curves were obtained at constant current densities of 0.25, 0.5, 1, 2 and 4 A g^{-1}. All the operating current densities were calculated based on the total weight of $NiCo_2O_4$–MnO_2 NWs with AG.

3. Results and discussion

3.1. Structure and morphology

Fig. 1 shows the composition and crystallite phase purity of the firecracker-like $NiCo_2O_4$–MnO_2 NWs. Almost all the identified peaks are indexed with the standard XRD pattern of spinel structure $NiCo_2O_4$ (JCPDS NO. 20-0781, Space group: F $\times$ 3 (202), lattice

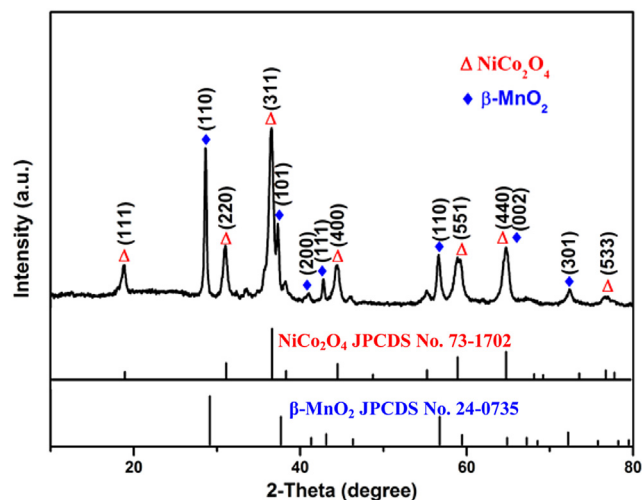**Fig. 1.** XRD pattern of the $NiCo_2O_4$–MnO_2 NWs.

constants: $a = b = c = 0.811$ nm) and β-MnO_2 (JCPDS NO. 24-0735, tetragonal symmetry with $P42/nm$ space group and lattice constants of $a = 4.399$ nm and $c = 2.874$ nm). No characteristic impurity peak is observed, indicating that the high-purity firecrackers-like $NiCo_2O_4$–MnO_2 NWs are produced by the simple co-precipitation method. Furthermore, the composition and crystallite phase of the pure MnOOH NWs are examined by X-ray powder diffraction (See Supplementary information, SI-1). All of the reflections of the XRD pattern can be readily indexed to a monoclinic phase MnOOH (manganite, JCPDS No: 41-1379).

As illustrated in Fig. 2a, the pure MnOOH NWs are prepared by a hydrothermal method. Subsequently, the pure MnOOH NWs are immersed into the reaction solution containing $Ni(NO_3)_2$, $Co(NO_3)_2$, NH_4F and urea. During the following hydrothermal crystallization process, the hydrolysis– precipitation process of NH_4F and urea takes place, which forms the rudiments of firecracker-like Ni, Co–hydroxide–carbonate (See Supplementary information, SI-2a). Deriving from the continuously proceeding reaction the rudiments of firecracker-like Ni, Co–hydroxide–carbonate were formed, and
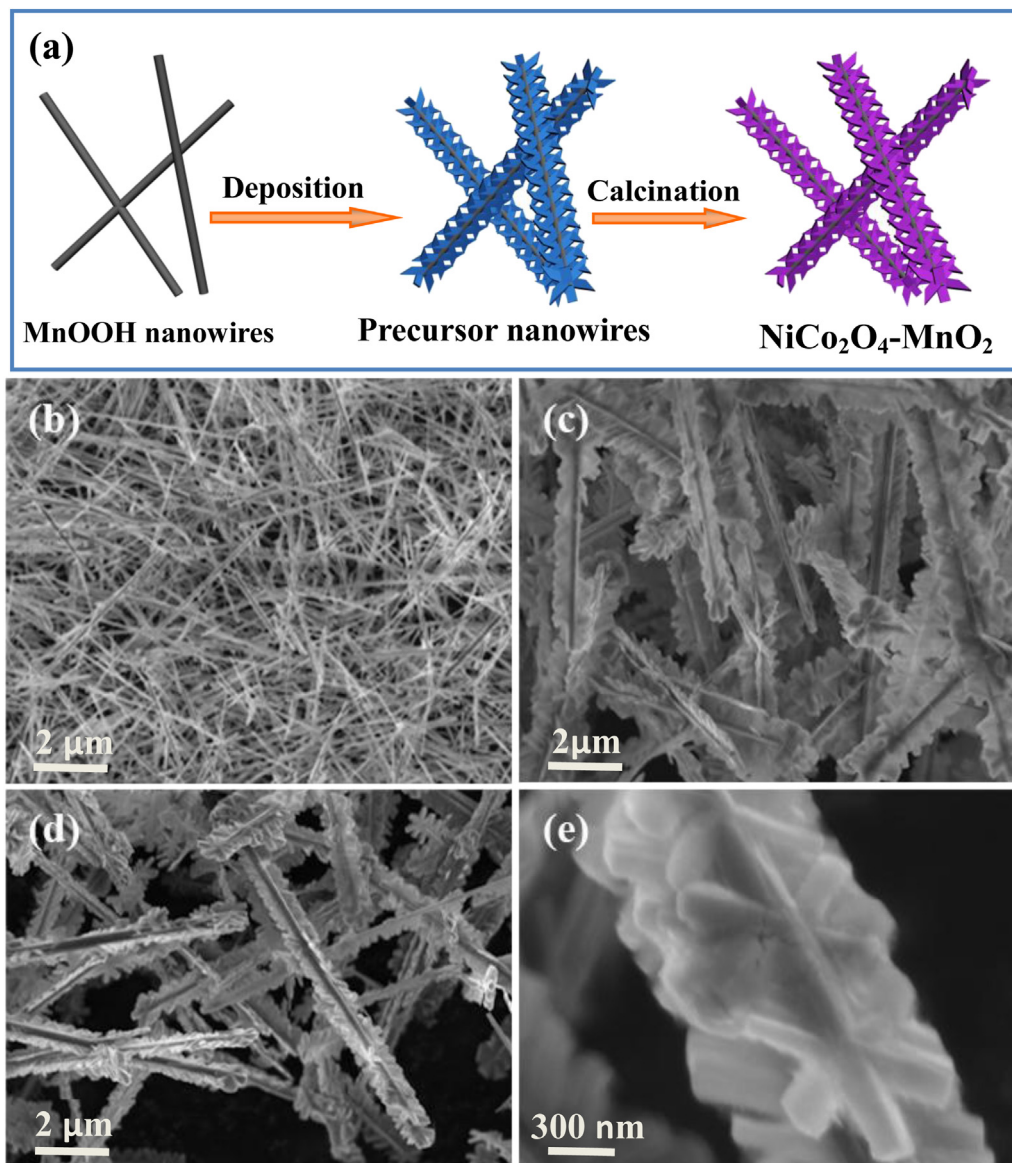

Fig. 2. (a) Schematic illustration of the synthesis of $NiCo_2O_4$–MnO_2 NWs, (b) SEM image of pure MnOOH nanowires, (c) SEM image of the precursor, (d, e) low-magnification and enlarged SEM images of the $NiCo_2O_4$–MnO_2 NWs.

then fully developed when the reaction time was prolonged (See Supplementary information, SI-2b and c). Moreover, increasing the reaction time to 18 h, the Ni, Co—hydroxide—carbonate is grown larger and the structure of nanowire is destroyed (See Supplementary information, SI-2d). Afterward, these precursor nanowires are annealed at 300 °C for 2 h, and $NiCo_2O_4$—MnO_2 NWs are obtained accordingly. Fig.2b shows SEM image of the pure MnOOH NWs. As shown in Fig 2b, it can be seen that the large-scale and uniform features of the pure MnOOH NWs. The average diameter of the MnOOH NWs is range of 100—150 nm, and the length can reach tens of micrometers. Fig. 2c shows that the hydroxide precursors are uniformly grown on MnOOH NWs. As shown in Fig. 2c, the every (Ni, Co) hydroxide precursor nanowires has uniform diameter of approximately 1 μm, which is much larger than that of pure MnOOH NWs. Moreover, the firecracker-like Ni—Co—hydroxide—carbonate have an average diameter of 200 nm and length up to around 400 nm. After heat treatment, the basic morphology of the sample is perfectly conserved without calcination-induced significant alterations (Fig. 2d and e). Interestingly, the firecracker-like Co_3O_4—MnO_2 NWs are also obtained in the absence of $Ni(NO_3)_2$ salt (See Supplementary information, SI-3 and SI-4). Moreover, we have done the experiment without MnO_2 NWs while keeping all the other conditions the same. What we obtained was the pure $NiCo_2O_4$ nanorods and Co_3O_4 nanosheets, respectively (See Supplementary information, SI-5).

The structural characteristics of the $NiCo_2O_4$—MnO_2 and Co_3O_4—MnO_2 NWs are further investigated by TEM (Fig. 3). Both the $NiCo_2O_4$—MnO_2 NWs (Fig. 3a) and Co_3O_4—MnO_2 NWs (Fig. 3d) consist of numerous interconnected nanoparticles and present a mesoporous structure, which is ascribed to the successive release and lose of CO_2 and H_2O during the thermal decomposition of precursor. It is well known that the mesoporous structures in nanosheets are important to facilitate the mass transport of electrolytes within the electrodes for fast redox reactions and double-layer charging/discharging. The porous structure will also greatly increase the electrode/electrolyte contact area, and thus further enhance the electrochemical performance. Fig. 3b is an HRTEM image of firecracker-like $NiCo_2O_4$ nanosheets. The spacing between adjacent fringes is ~0.47 nm, close to the theoretical interplane spacing of spinel $NiCo_2O_4$ (111) planes. The selected area electron diffraction (SAED) pattern (Fig. 3c) indicates the polycrystalline nature of the nanosheets, and the diffraction rings can be readily indexed to the (200), (311), (400), and (440) planes of the $NiCo_2O_4$ phase, which is consistent with the above XRD result. Fig. 3e is an HRTEM image of firecracker-like Co_3O_4 nanosheets. The lattice fringes show the structural characteristic of the cubic spinel Co_3O_4 crystal, in which the d-spacings of 0.29 and 0.24 nm correspond to the distance of the (220) and (311) planes, respectively. The SAED pattern shows well-defined diffraction rings, suggesting their polycrystalline characteristics.

The nitrogen adsorption and desorption isotherms of the $NiCo_2O_4$—MnO_2 and Co_3O_4—MnO_2 NWs are shown in Fig. 4. The N_2 adsorption—desorption isotherm is characteristic of type IV with a type H3 hysteresis loop which mostly corresponds to the presence of aggregated particles with slit shape pores [24,25,26,27]. The Brunauer—Emmett—Teller (BET) surface area values of the $NiCo_2O_4$—MnO_2 and Co_3O_4—MnO_2 NWs are calculated to be 60.02 and 35.24 m^2 g^{-1}, respectively. The pore size distribution of the sample calculated by desorption isotherm using Barret—Joyner—Halenda (BJH) method is shown in inset of Fig. 4. The average pore diameters of $NiCo_2O_4$—MnO_2 and Co_3O_4—MnO_2 NWs are found to be in the mesopore region. However, the pore size distribution maximum of the samples are centered at nearly same pore radii, for $NiCo_2O_4$—MnO_2 NWs, it is centered at 3.67 nm, for Co_3O_4—MnO_2 NWs at 3.29 nm. These results show that mesopores of nearly same sizes originate from the nanostructures. The intensities of the pore size distribution in $NiCo_2O_4$—MnO_2 NWs are slightly higher than that of Co_3O_4—MnO_2 NWs, suggesting higher pore volume of
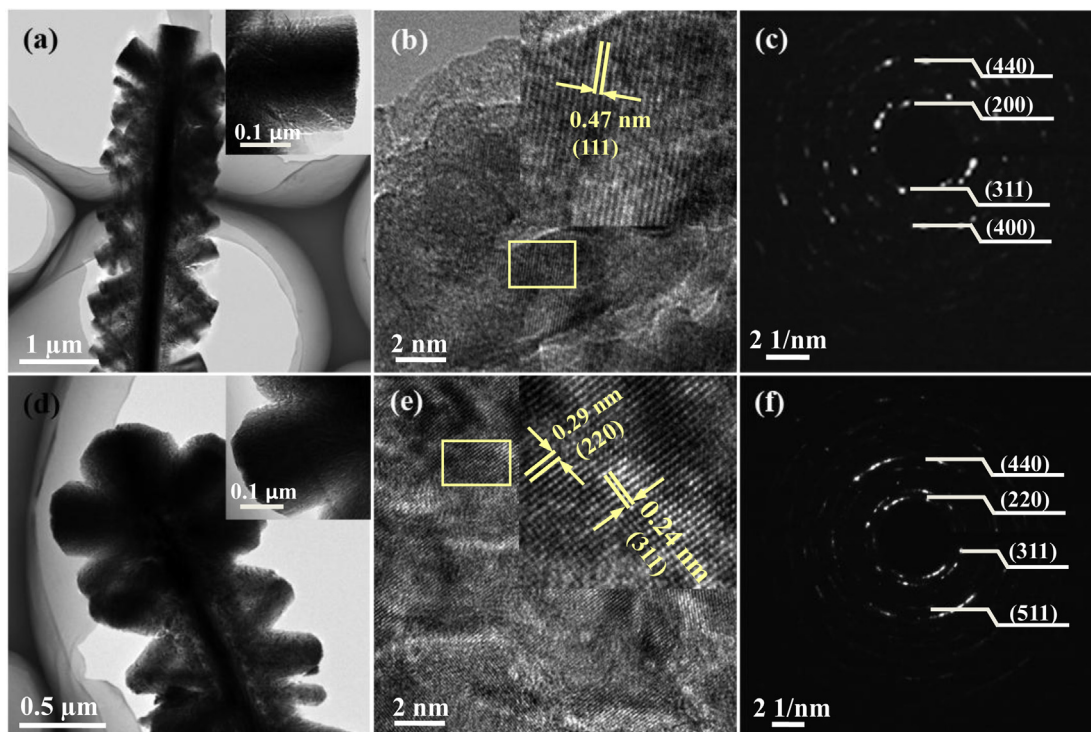
Fig. 3. TEM images of the $NiCo_2O_4$—MnO_2 NWs(a) and Co_3O_4—MnO_2 NWs(d), HRTEM images of the $NiCo_2O_4$—MnO_2 NWs(b) and Co_3O_4—MnO_2 NWs(e), SAED patterns of the $NiCo_2O_4$—MnO_2 NWs (c) and Co_3O_4—MnO_2 NWs(f).
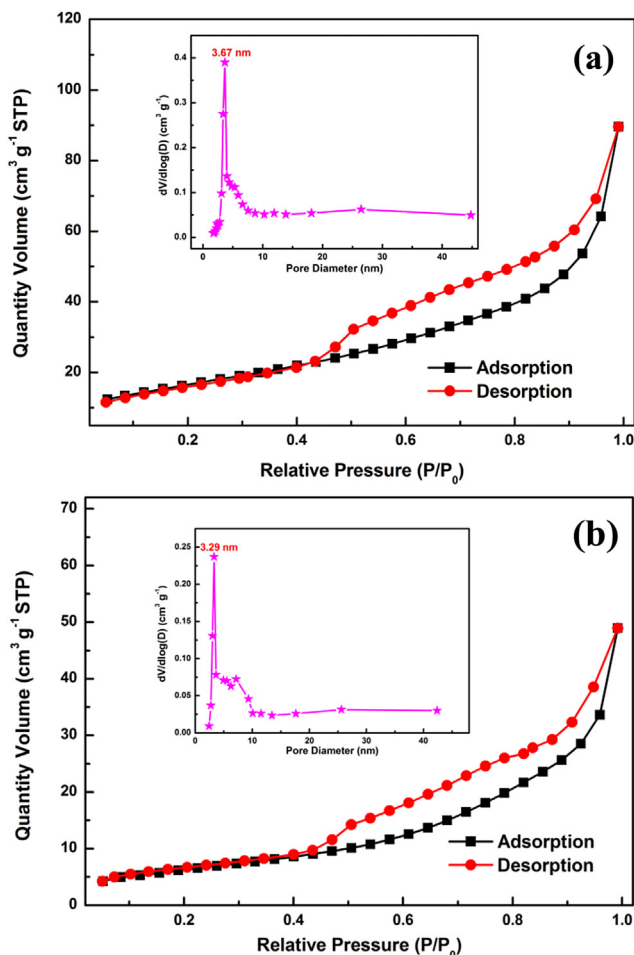
Fig. 4. Nitrogen adsorption and desorption isotherms for the $NiCo_2O_4$–MnO_2 NWs (a) and Co_3O_4–MnO_2 NWs (b). The insets show the corresponding BJH pore size distributions.

$NiCo_2O_4$–MnO_2 NWs. The pore volume of Co_3O_4–MnO_2 NWs is calculated as 0.082 cm^3 g^{-1}, while the pore volume of $NiCo_2O_4$–MnO_2 NWs is up to 0.139 cm^3 g^{-1}. In conclusion, high surface area and large pore volume are achieved for $NiCo_2O_4$–MnO_2 NWs, so it is expected that the $NiCo_2O_4$–MnO_2 NWs may exhibit improved electrochemical performance compared to Co_3O_4–MnO_2 NWs, and further electrochemical measurements have been carried out to prove this hypothesis.

3.2. Electrochemical performances

In order to compare the contribution of $NiCo_2O_4$ and Co_3O_4 to the electrochemical performance of the electrode materials, cyclic voltammetry (CV), galvanostatic charge–discharge (GCD) and electrochemical impedance spectroscopy (EIS) measurements in a three-electrode system are employed. Representative CV curves for the $NiCo_2O_4$–MnO_2 and Co_3O_4–MnO_2 NWs in three electrode configuration at different scan rates are shown in Fig. 5a and b. As compared with CV curves of the $NiCo_2O_4$–MnO_2 NWs, the Co_3O_4–MnO_2 NWs has more distinct redox peaks. However, the area under the CV curve of the $NiCo_2O_4$–MnO_2 NWs is clearly much larger than that of the Co_3O_4–MnO_2 NWs at the same scan rate. It is well-known that the specific capacitance is proportional to the area of the CV curve [10,28]. Thus, the $NiCo_2O_4$–MnO_2 NWs has higher capacitances than the Co_3O_4–MnO_2 NWs.

In order to investigate the capability of the materials, the GCD tests of the $NiCo_2O_4$–MnO_2 and Co_3O_4–MnO_2 NWs are carried out at different constant current densities (Fig. 5c and d). The curve of $NiCo_2O_4$–MnO_2 NWs is linear and symmetric, indicating an ideal capacitor capable of reversible charging and discharging [29,30]. In comparison, the curve of Co_3O_4–MnO_2 NWs is distorted to some extent. Low internal resistance is very favorable in energy storage devices, which reduces energy waste during charging/discharging processes [31,32]. The increase in the charging time represents the higher capacitance of the $NiCo_2O_4$–MnO_2 NWs. According to the GCD curves, the specific capacitances of the electrodes are respectively calculated using the following equation [33]:

$$C_m = \frac{I\Delta t}{m\Delta V}$$

where m, I, Δt and ΔV are the weight (g) of the electroactive materials, discharge current (A), the discharging time (s), and the discharging potential range (V), respectively. The specific capacitances of $NiCo_2O_4$–MnO_2 and Co_3O_4–MnO_2 NWs are 343 F g^{-1} and 192 F g^{-1} at a current density of 0.5 A g^{-1}, respectively, which is much higher than the pure MnO_2 NWs (14 F g^{-1}), $NiCo_2O_4$ nanorods (102 F g^{-1}) and Co_3O_4 nanosheets (77 F g^{-1}) (See Supplementary information, SI-6). Maximizing the utilization of active materials is always considered as a challenge because only the surface of oxides can be utilized for charge storage. Up to now, the $NiCo_2O_4$-based electrodes with various substrates and nanostructure have been prepared to improve the utilization of $NiCo_2O_4$. Thus, the comparison of the specific capacitance based on the mass of $NiCo_2O_4$ (the mass of $NiCo_2O_4$ was obtained by chemical analysis) alone between this work and previous reports is summarized (See Supplementary information, Table S1). According to the comparison in Table S1, it can be obtained that the specific capacitance based on the in our work is 798 F g^{-1}, indicating that the specific capacitance of firecracker-like $NiCo_2O_4$–MnO_2 NWs nanostructure in this work can actually be higher than many $NiCo_2O_4$ nanostructures-based supercapacitors previously reported.

The specific capacitance of $NiCo_2O_4$–MnO_2 and Co_3O_4–MnO_2 NWs electrodes at various current densities is shown in Fig. 5e. We observe that the specific capacitance for both electrodes decreases with an increase in the current density from 0.5 A g^{-1} to 8 A g^{-1}. This is a common phenomenon, caused by the insufficient time available for ion diffusion at high current density [34]. In addition, the $NiCo_2O_4$–MnO_2 NWs maintains its 75.3% capacitance as the current density is increased from 0.5 to 8 A g^{-1}, while the Co_3O_4–MnO_2 NWs lose 30% of its capacity in the same condition, indicating that the $NiCo_2O_4$–MnO_2 NWs have better rate capability, in good accordance with the CV tests.

The EIS analysis has been recognized as one of the principal methods for examining the fundamental behavior of electrode materials, which not only provides useful information on the electrochemical frequency of the system but also allows for the measurement of redox reaction resistance and equivalent series resistance of the electrode [15,35]. Typical Nyquist plots of the $NiCo_2O_4$–MnO_2 and Co_3O_4–MnO_2 NWs electrode are shown in Fig. 5f. The two impedance spectra are composed of a semicircular arc in the high-frequency range and a straight line in the low-frequency range. The intersection of the plot at the x-axis represents the solution resistance (R_s), which includes the following three terms: the resistance of the KOH aqueous solution, the intrinsic resistance of the electroactive materials and the contact resistance at the interface between electroactive materials and current collector [31,36]. As can be seen from the inset, the calculated R_s values are 0.46 and 0.48 Ω for $NiCo_2O_4$–MnO_2 and Co_3O_4–MnO_2 NWs electrode, respectively, it's much lower than
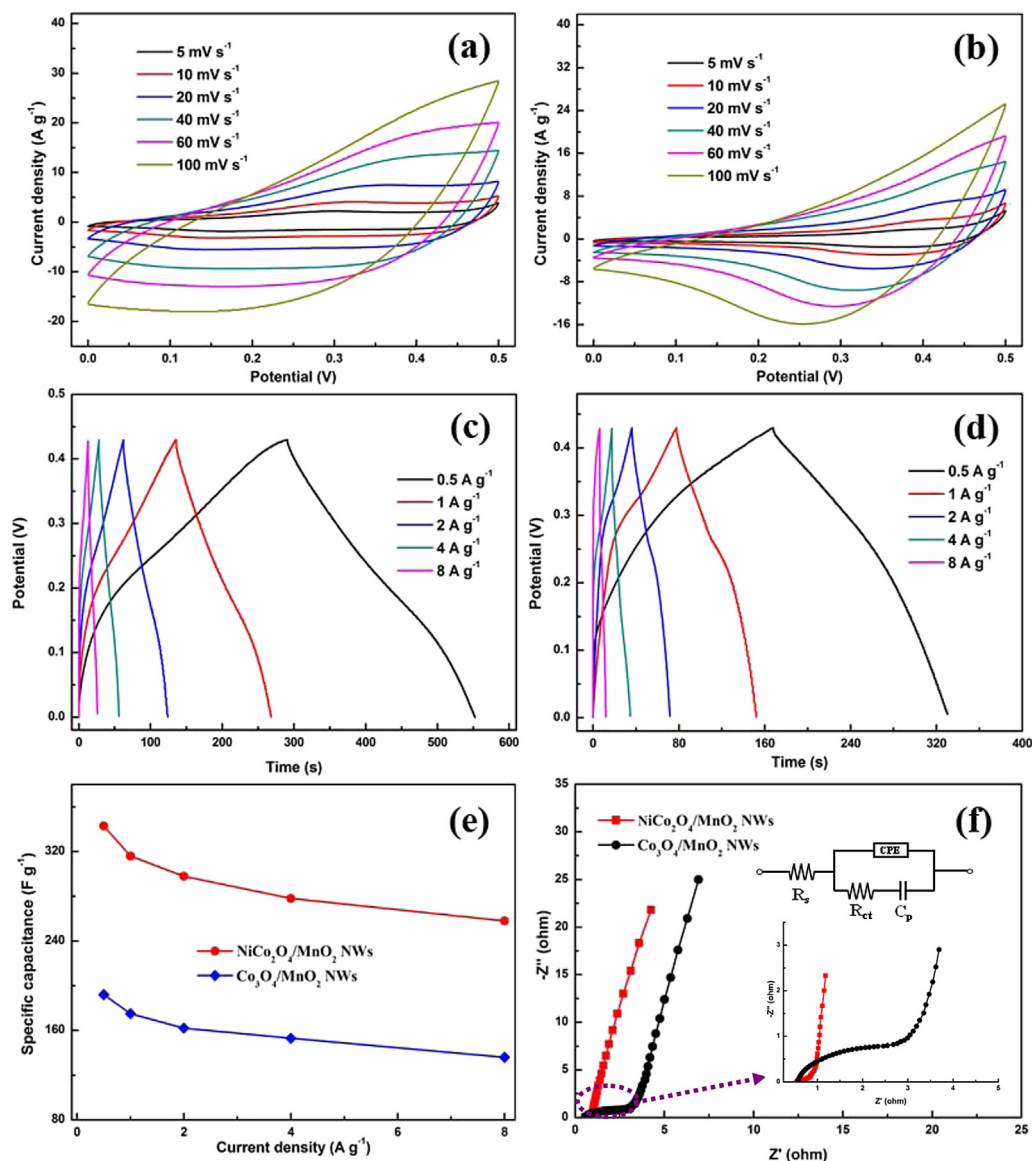
Fig. 5. Electrochemical evaluations of the NiCo$_2$O$_4$–MnO$_2$ and Co$_3$O$_4$–MnO$_2$ NWs: (a, b) CV curves, (c, d) charge–discharge curves, (e) capacitances versus current densities, and (f) Nyquist plots (Insert show the enlarged part of Nyquist plots and equivalent circuit for the electrochemical impedance spectrum).

that of pure NiCo$_2$O$_4$ and Co$_3$O$_4$ (See Supplementary information, SI-7). At the high frequencies, semicircles can be observed for both with the diameters representing the charge-transfer resistance (R_{ct}). R_{ct} can be directly measured from the Nyquist plots as the semicircular arc diameter. The calculated R_{ct} values for NiCo$_2$O$_4$–MnO$_2$ and Co$_3$O$_4$–MnO$_2$ NWs electrode are 0.8 Ω and 1.6 Ω respectively. The NiCo$_2$O$_4$–MnO$_2$ NWs electrodes have a low R_{ct} value compared with the Co$_3$O$_4$–MnO$_2$ NWs electrode, resulting in an improved charge transfer performance for the electrode. The straight line in the low-frequency range is called the Warburg resistance (W), which is caused by the frequency dependence of ion diffusion/transport from the electrolyte to the electrode surface [37,38]. As shown in Fig. 5f, NiCo$_2$O$_4$–MnO$_2$ NWs electrode has a smaller Warburg region, presenting a minor Warburg resistance. It implies that the highly porous NiCo$_2$O$_4$–MnO$_2$ NWs electrode is able to facilitate the penetration of electrolyte, leading to fast diffusion of electrolyte into the pores of NiCo$_2$O$_4$ [39]. It can be seen that the slope of the straight line for NiCo$_2$O$_4$–MnO$_2$ NWs electrode are much larger than that of the Co$_3$O$_4$–MnO$_2$ NWs electrode. This

observation indicates that the NiCo$_2$O$_4$–MnO$_2$ NWs electrode has much lower diffusive resistance than that of the Co$_3$O$_4$–MnO$_2$ NWs.

Long cycle life for the supercapacitors is an important parameter for their practical application. Supercapacitors should work steadily and safely, which requires the specific capacitance of electrode materials to change as little as possible. The relationship of the specific capacitance and Coulombic efficiency against cycling number of the NiCo$_2$O$_4$–MnO$_2$ NWs electrode is shown in Fig. 6a. The specific capacitance of NiCo$_2$O$_4$–MnO$_2$ NWs electrode decreases gradually with increasing cycle numbers and its capacitance retention is 89.7% after 3000 cycles. Such excellent cycling stability is mainly attributed to the following aspects. First, the synergistic contribution from NiCo$_2$O$_4$ and MnO$_2$, both the firecracker-like NiCo$_2$O$_4$ nanosheets and the MnO$_2$ nanowires can have redox reactions with anions and cations from the electrolyte, respectively, accounting for the electrochemical charge storage. Second, the MnO$_2$ nanowires provides a direct pathway for electron transport while the partial connected NiCo$_2$O$_4$ nanosheets with high specific surface area provide more electronic transmission channels (as schematically illustrated in
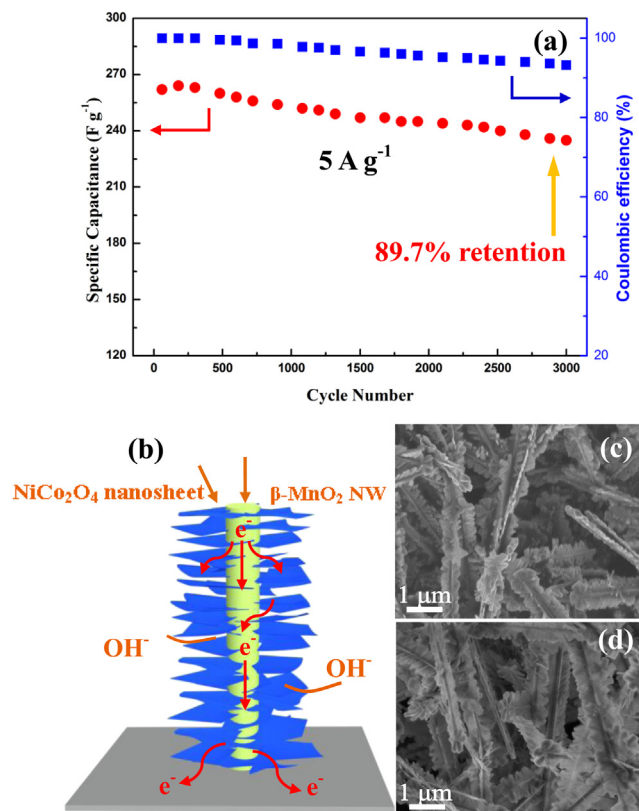
Fig. 6. (a) Variation of capacitance with cycle number at 5 A g^{-1}, (b) schematic of the charge storage advantage of the NiCo$_2$O$_4$–MnO$_2$ NWs, (c) and (d) SEM images of the NiCo$_2$O$_4$–MnO$_2$ NWs before and after 3000 cycles.
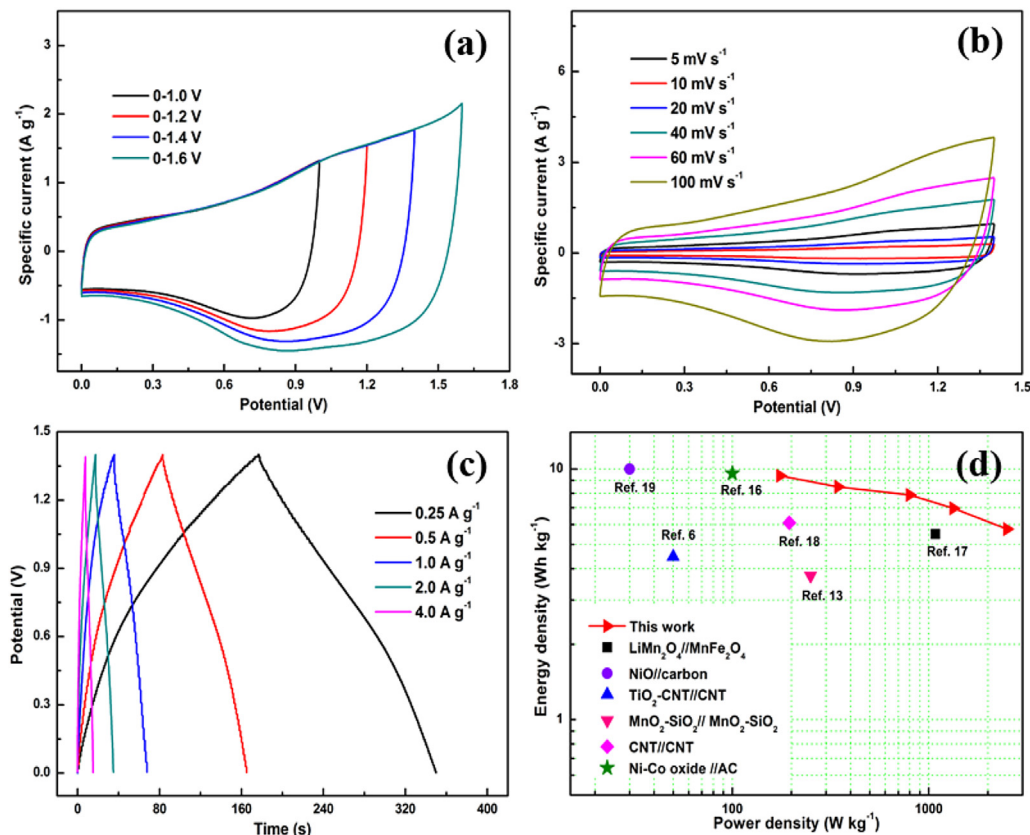
Fig. 6b). Third, the firecracker-like NiCo$_2$O$_4$–MnO$_2$ possess higher pore volume, which is probably more beneficial to double-layer capacitor. Furthermore, the more porous of firecracker-like NiCo$_2$O$_4$–MnO$_2$ also provides more channel for electrolyte. So the cycle performance can be enhanced by the fast ion diffusion in the one-dimensional nanoporous architecture.

After long-term cycling, the firecracker-like NiCo$_2$O$_4$–MnO$_2$ NWs are overall preserved with little structure deformation, as shown in Fig. 6c and d. On the other hand, it is noted that the Coulombic efficiency of the NiCo$_2$O$_4$–MnO$_2$ NWs can maintain almost 93% after long-term cycling. These results demonstrate the as-prepared NiCo$_2$O$_4$–MnO$_2$ NWs are very stable as an active electrode material. By contrast, Co$_3$O$_4$–MnO$_2$ NWs electrode lose 26.2% of its capacitance after 3000 cycles with the same current density (See Supplementary Information, SI-8) and the structure of firecracker-like Co$_3$O$_4$–MnO$_2$ NWs is slight destroyed after 3000 cycles.

The as-assembled NiCo$_2$O$_4$–MnO$_2$//AG asymmetric cell is measured at different potential windows in a 2 M KOH aqueous electrolyte at a scan rate of 40 mV s^{-1}, and the resulted CV curves are exhibited in Fig. 7a. The CV curves show a quasi-rectangular shape from 1.0 V to 1.4 V. At a potential window of 1.6 V, the CV curve shows a distortion and a slight hump around 1.6 V. This indicates that some irreversible reactions happen when the potential window is higher than 1.4 V. Thus, the optimum working potential window for this asymmetric supercapacitor is from 0 to 1.4 V Fig. 7b shows the typical CV curves of the asymmetric cell in the voltage window from 0 to 1.4 V at the scan rates of 5, 10, 20, 50 and 100 mV s^{-1}. The CV profile of the asymmetric cell remains relatively quasi-rectangular at a high scan rate of 100 mV s^{-1}, demonstrating good charge/discharge properties and rate capability of the asymmetric supercapacitor [7,40]. To further evaluate the electrochemical performance of the asymmetric cell, galvanostatic

Fig. 7. (a) CV curves of the NiCo$_2$O$_4$–MnO$_2$//AG asymmetric supercapacitor cell measured at different potential windows in 2 M KOH electrolyte, (b) CV curves of the NiCo$_2$O$_4$–MnO$_2$//AG asymmetric supercapacitor cell measured at different scan rates,(c) charge–discharge curves of the NiCo$_2$O$_4$–MnO$_2$//AG asymmetric supercapacitor, (d) a Ragone plot of the NiCo$_2$O$_4$–MnO$_2$//AG asymmetric supercapacitor.

charge–discharge tests are performed. As shown in Fig. 7c, these typical triangular-shape charge/discharge curves exhibit good symmetry and fairly linear slopes at different current densities, again demonstrating the ideal capacitive characteristic. The specific capacitance of the $NiCo_2O_4$–MnO_2//AG asymmetric cell is calculated to be 31.3 F g^{-1} based on the total weight of the electrodes at a current density of 0.25 A g^{-1}, and still maintains at 24 F g^{-1} when the current density increases by as much as 16 times (4 A g^{-1}). To further illustrate the energy and power property of this asymmetric supercapacitor, a Ragone plot is shown in Fig. 7. This device shows a high energy density of 9.4 Wh kg^{-1} at a power density of 175 W kg^{-1}, while maintaining a high energy density of 5.8 Wh kg^{-1} at a power density of 2500 W kg^{-1}. This result shows a much improved energy density at high power density compared with a Ni–Co oxide//AC asymmetric device (12 Wh kg^{-1} at 95 W kg^{-1}) [41], a MnO_2-modified diatomites//MnO_2-modified diatomites symmetric device (3.75 Wh kg^{-1} at 250 W kg^{-1}) [42], a CNT//CNT symmetric device (6.1 Wh kg^{-1} at 195 W kg^{-1}) [43], a NiO//carbon asymmetric device (~10 Wh kg^{-1} at 30 W kg^{-1}) [44], a TiO_2-CNT//CNT asymmetric device (4.47 Wh kg^{-1} at 50 W kg^{-1}) [45], and a $LiMn_2O_4$//$MnFe_2O_4$ asymmetric device (5.5 Wh kg^{-1} at 1080 W kg^{-1}) [46].

4. Conclusion

In summary, to bypass the lower electrical conductivity by Co_3O_4–MnO_2 NWs electrode, we have successfully fabricated firecrackers-like $NiCo_2O_4$–MnO_2 NWs via the simple co-precipitation method followed by annealing in atmosphere. Electrochemical measurements reveal that the $NiCo_2O_4$–MnO_2 NWs electrode exhibits much higher specific capacitance and better rate capability compared with Co_3O_4–MnO_2 NWs electrode. Specifically, the $NiCo_2O_4$–MnO_2 NWs electrode displays a high specific capacitance of 343 F g^{-1} at current density of 0.5 A g^{-1}, excellent cycle stability with capacitance retention of 89.7% at 5 A g^{-1} after 3000 cycles. Furthermore, the $NiCo_2O_4$–MnO_2//AG asymmetric cell delivers an energy density of 9.4 Wh kg^{-1} and a maximum power density of 2.5 kW kg^{-1}, indicating a promising potential application as an effective candidate for supercapacitors. The superior capacitive performance of $NiCo_2O_4$–MnO_2 NWs electrode is attributed to the high electrical conductivity, short electron transporting path, with Ni-substitution and good contact.

Acknowledgments

Appendix A. Supplementary data

Supplementary data related to this article can be found at http://dx.doi.org/10.1016/j.jpowsour.2014.07.144.

References

[1] M. Huang, Y. Zhang, F. Li, L. Zhang, R.S. Ruoff, Z. Wen, Q. Liu, Sci. Rep. 4 (2014) 3878, 1–7.
[2] Y. Liu, D. Yan, R. Zhuo, S. Li, Z. Wu, J. Wang, P. Ren, P. Yan, Z. Geng, J. Power Sources 242 (2013) 78–85.
[3] C. Liu, Z. Yu, D. Neff, A. Zhamu, B.Z. Jang, Nano Lett. 10 (2010) 4863–4868.
[4] M.-G. Jeong, K. Zhuo, S. Cherevko, W.-J. Kim, C.-H. Chung, J. Power Sources 244 (2013) 806–811.
[5] M. Huang, Y. Zhang, F. Li, L. Zhang, Z. Wen, Q. Liu, J. Power Sources 252 (2014) 98–106.
[6] S. Wu, W. Chen, L. Yan, J. Mater. Chem. A 2 (2014) 2765–2772.
[7] P. Yang, Y. Li, Z. Lin, Y. Ding, S. Yue, C.P. Wong, X. Cai, S. Tan, W. Mai, J. Mater. Chem. A 2 (2014) 595–599.
[8] Y. Luo, D. Kong, J. Luo, S. Chen, D. Zhang, K. Qiu, X. Qi, H. Zhang, C.M. Li, T. Yu, RSC Adv. 3 (2013) 14413–14422.
[9] J. Li, W. Zhao, F. Huang, A. Manivannan, N. Wu, Nanoscale 3 (2011) 5103–5109.
[10] J.-H. Zhong, A.-L. Wang, G.-R. Li, J.-W. Wang, Y.-N. Ou, Y.-X. Tong, J. Mater. Chem. 22 (2012) 5656–5665.
[11] L. Jiang, R. Zou, W. Li, J. Sun, X. Hu, Y. Xue, G. He, J. Hu, J. Mater. Chem. A 1 (2013) 478–481.
[12] P. Roy, S. Berger, P. Schmuki, Angew. Chem. Int. Ed. 50 (2011) 2904–2939.
[13] X. Lu, M. Yu, G. Wang, T. Zhai, S. Xie, Y. Ling, Y. Tong, Y. Li, Adv. Mater. 25 (2013) 267–272.
[14] Y. Wang, Z. Hong, M. Wei, Y. Xia, Adv. Funct. Mater. 22 (2012) 5185–5193.
[15] L. Huang, D. Chen, Y. Ding, S. Feng, Z.L. Wang, M. Liu, Nano Lett. 13 (2013) 3135–3139.
[16] X. Liu, S. Shi, Q. Xiong, L. Li, Y. Zhang, H. Tang, C. Gu, X. Wang, J. Tu, ACS Appl. Mater. Interfaces 5 (2013) 8790–8795.
[17] C. Yuan, J. Li, L. Hou, X. Zhang, L. Shen, X.W. Lou, Adv. Funct. Mater. 22 (2012) 4592–4597.
[18] C. Yuan, J. Li, L. Hou, J. Lin, X. Zhang, S. Xiong, J. Mater. Chem. A 1 (2013) 11145–11151.
[19] C. Yuan, J. Li, L. Hou, J. Lin, G. Pang, L. Zhang, L. Lian, X. Zhang, RSC Adv. 3 (2013) 18573–18578.
[20] C.-T. Hsu, C.-C. Hu, J. Power Sources 242 (2013) 662–671.
[21] H. Jiang, J. Ma, C. Li, Chem. Commun. 48 (2012) 4465–4467.
[22] R. Zou, K. Xu, T. Wang, G. He, Q. Liu, X. Liu, Z. Zhang, J. Hu, J. Mater. Chem. a 1 (2013) 8560–8566.
[23] H. Wang, X. Wang, ACS Appl. Mater. Interfaces 5 (2013) 6255–6260.
[24] H. Jiang, C. Li, T. Sun, J. Ma, Chem. Commun. 48 (2012) 2606–2608.
[25] Y. Qin, F. Zhang, Y. Chen, Y. Zhou, J. Li, A. Zhu, Y. Luo, Y. Tian, J. Yang, J. Phys. Chem. C 116 (2012) 11994–12000.
[26] G. Zhang, W. Li, K. Xie, F. Yu, H. Huang, Adv. Funct. Mater. 23 (2013) 3675–3681.
[27] Z. Zhang, H. Che, Y. Wang, L. Song, Z. Zhong, F. Su, Catal. Sci. Technol. 2 (2012) 1953–1960.
[28] H. Chen, J. Jiang, L. Zhang, H. Wan, T. Qi, D. Xia, Nanoscale 5 (2013) 8879–8883.
[29] Y. Jin, H. Chen, M. Chen, N. Liu, Q. Li, ACS Appl. Mater. Interfaces 5 (2013) 3408–3416.
[30] P. Yang, Y. Ding, Z. Lin, Z. Chen, Y. Li, P. Qiang, M. Ebrahimi, W. Mai, C.P. Wong, Z.L. Wang, Nano Lett. 14 (2014) 731–736.
[31] G. Zhu, Z. He, J. Chen, J. Zhao, X. Feng, Y. Ma, Q. Fan, L. Wang, W. Huang, Nanoscale 6 (2014) 1079–1085.
[32] G. Zhang, X.W. Lou, Adv. Mater. 25 (2013) 976–979.
[33] M. Hakamada, A. Moriguchi, M. Mabuchi, J. Power Sources 245 (2014) 324–330.
[34] G. Zhang, X.W. Lou, Sci. Rep. 3 (2013) 1470–1476.
[35] Z. Tang, C.-h. Tang, H. Gong, Adv. Funct. Mater. 22 (2012) 1272–1278.
[36] J. Zhang, X.S. Zhao, Carbon 52 (2013) 1–9.
[37] T. Zhai, F. Wang, M. Yu, S. Xie, C. Liang, C. Li, F. Xiao, R. Tang, Q. Wu, X. Lu, Y. Tong, Nanoscale 5 (2013) 6790–6796.
[38] Q. Wang, J. Xu, X. Wang, B. Liu, X. Hou, G. Yu, P. Wang, D. Chen, G. Shen, ChemElectroChem 1 (2014) 559–564.
[39] A. Ramadoss, S.J. Kim, Carbon 63 (2013) 434–445.
[40] J.-G. Wang, Y. Yang, Z.-H. Huang, F. Kang, Electrochim. Acta 56 (2011) 9240–9247.
[41] C. Tang, Z. Tang, H. Gong, J. Electrochem. Soc. 159 (2012) A651–A656.
[42] Y.X. Zhang, M. Huang, F. Li, X.L. Wang, Z.Q. Wen, J. Power Sources 246 (2014) 449–456.
[43] Q. Wang, Z.H. Wen, J.H. Li, Adv. Funct. Mater. 16 (2006) 2141–2146.
[44] D.-W. Wang, F. Li, H.-M. Cheng, J. Power Sources 185 (2008) 1563–1568.
[45] X. Sun, M. Xie, J.J. Travis, G. Wang, H. Sun, J. Lian, S.M. George, J. Phys. Chem. C 117 (2013) 22497–22508.
[46] Y.-P. Lin, N.-L. Wu, J. Power Sources 196 (2011) 851–854.